

# A numerical study of third-order equation with time-dependent coefficients: KdVB equation

Cristhian Montoya<sup>a</sup>, Carlos Spa<sup>b</sup>

<sup>a</sup>*School of Applied Sciences and Engineering, Universidad EAFIT, Medellín, Colombia.*

<sup>b</sup>*CASE department in the Barcelona Supercomputing Center. Plaza Eusebi Güell n3. Barcelona. Spain*

---

## Abstract

In this article we present a numerical analysis for a third-order differential equation with non-periodic boundary conditions and time-dependent coefficients, namely, the linear Korteweg–de Vries Burgers equation. This numerical analysis is motivated due to the dispersive and dissipative phenomena that govern this kind of equations. This work builds on previous methods for dispersive equations with constant coefficients, expanding the field to include a new class of equations which until now have eluded the time-evolving parameters. More precisely, throughout the Legendre–Petrov–Galerkin method we prove stability and convergence results of the approximation in appropriate weighted Sobolev spaces. These results allow to show the role and trade off of these temporal parameters into the model. Afterwards, we numerically investigate the dispersion–dissipation relation for several profiles, further provide insights into the implementation method, which allow to exhibit the accuracy and efficiency of our numerical algorithms.

*Keywords:* Korteweg–de Vries Burgers equation, Legendre–Petrov–Galerkin method, stability analysis, convergence, time-dependent coefficients

---

## 1. Introduction

Since the Orszag’s pioneer works in the early seventies [17], several numerical spectral methods for solving initial value problems of partial differential equations (PDEs) have become increasingly popular in recent years, specially those associated to spectral Galerkin approximations. As it is well known, the spectral methods involve representation the solutions as a truncated series of known functions of the independent variables. In addition, due to the high-order accuracy whenever they work, these methods are preferable in numerical solutions of PDEs. In that framework, Jacobi polynomials [34] have been used in a variety of applications due to their ability to approximate general classes of functions as well as to its orthogonality properties; for instance, in resolution of the Gibbs’ phenomenon [18], transverse vibrations in beams and plates [5], electrocardiogram data compression [30, 35], and solution to even-order differential equations subject to various boundary conditions [7, 8, 10].

For the class of odd-order differential equations, which only includes a dispersive process, such as the Korteweg–de Vries (KdV) equation [24], it is well known that periodic boundary conditions onto those models allow for example to apply the Fourier spectral method for obtaining stability results and error estimates, see for instance, Fornberg and Whitham [14], Fenton and Rienecker [13], Maday and Quarteroni [29], Deng and Ma [6], and references therein. Nevertheless, by considering a bounded domain with non-periodic boundary conditions on those models, polynomial spectral schemes based in Jacobi polynomials have been successfully used for their numerical approximations in space [1, 27, 28, 25, 19, 32, 23]. A common characteristic in the previous papers is the Petrov–Galerkin formulation, which appears due to the lack of symmetry of the main operator and simultaneously incorporates the boundary conditions inside the polynomial bases. This fact allow to integrate by parts freely in space omitting any additional boundary terms. In addition, it is worth mentioning the hybrid method proposed by Ma and Sun [27], where the linear part of the KdV equation was treated by a Legendre–Petrov–Galerkin (LPG) method, and the nonlinear term was treated using a Chebyshev–collocation method. Moreover, they showed an estimate of order  $N^{-r}$ ,  $r \geq 2$  in  $L^2$ -norm (i.e.,

$N$  is the number of modes) for the linear KdV equation when the solutions satisfy a suitable regularity. Indeed, [27] constitutes a starting point in our analysis.

By incorporating a second-order term into the model, it might add a dissipative phenomenon such as occurs in Burgers-type equations [3]. The resultant equation is the so-called Korteweg-de Vries-Burgers (KdVB) equation. In [33], Shen first introduced a dual LPG method for the KdVB equation, where the innovation lies in the choice of both trial and test spaces, which form a sequence of orthogonal polynomials in weighted Sobolev spaces. This fact allow to establish optimal error estimates in appropriate Sobolev spaces. More precisely, in that paper, for the linear KdVB equation with constant coefficients, the author proven a rate of convergence of order  $(1 + |\beta|N)N^{1-r}$ ,  $r \geq 1$ , where  $\beta \in (-\frac{1}{3}, \frac{1}{6})$  is the coefficient associated to the second-order term (in some cases it can represent the viscosity constant). Afterwards, Yuan et al. [39] extended the method proposed by Shen to fifth-order KdV-type equations. On the other hand, by using Jacobi polynomials, Doha et al. [9] proposed numerical schemes for solving both third and fifth-order differential equations with space-dependent coefficients, although no theoretical result have been provided.

Respect to the time discretization, a classical Crank-Nicholson-leap-frog scheme describes a good convergence property for the nonlinear cases in many of the above papers, meanwhile, a forward Euler scheme is enough for the linear model. However, it should be pointed out that, in all previous approaches, they have obtained either numerical or theoretical results assuming always that both the dispersion and dissipation parameters are time-independent coefficients.

In general aspects, the ability to explicitly express the time-parametric dependence of coefficients in a dynamic system is necessary for accurate and quantitative characterization of partial differential equations. In practice this is an important innovation since the parameters of physical systems often vary during the measurement process, so that the parametric dependencies may be disambiguated from the model itself. Motivated by this, our work builds on previous methods for dispersive equations with constant coefficients, expanding the field to include a new class of equations which until now have eluded the time-evolving parameters. In fact, in contrast to the previous works, in this paper we consider a third-order equation with time-dependent coefficients, namely, the KdVB equation with non-periodic boundary conditions. To the best of our knowledge, in the literature no rigorous analysis of stability and convergence of a numerical scheme exists with time-dependent coefficients for this model. The inclusion of dispersive and dissipative parameters with temporal dependence makes a more careful treatment of the numerical approximation, giving now a first theoretical answer to the relation between them, as well as indicating appropriate ranges where the solutions can be tested in order to obtain desired rate of error. Thus our method takes as starting point the framework proposed in [27], in this way, the first goal of this paper is to construct the LPG scheme for the KdVB equation with time varying coefficients. At this point, it is worth mentioning that under this setting, one main advantage is the use of few number of modes for obtaining good numerical simulations. Additionally, our error analysis show that the convergence rate is suboptimal respect to diffusion parameters, while, for dispersion parameters, the convergence is optimal. It is consistent with the results above mentioned and studied in [27, 33] for constant coefficients. Nevertheless, due to the parametric dependency, our estimates are carried out by considering an appropriate relation among the variable time coefficients, which in turn shows a strong correlation between those coefficients and the LPG method.

The remainder of this paper is organized as follows. In Section 2, we develop a fully discrete approximation for the KdVB equation with time-varying coefficients, further, we prove stability and convergence estimates in weighted Sobolev spaces. In Section 3, we numerically investigate the dispersion-dissipation relation for several profiles, and providing insights into the implementation method. Finally, in the last section, we present the conclusions and outlooks.

## 2. Method and theoretical results

In this section we study the numerical approximation for third-order differential equations with non-periodic boundary conditions, which in turn include time-dependent coefficients. Specifically, we consider equations of the form

$$\begin{cases} \partial_t u + \alpha(t)\partial_x^3 u - \beta(t)\partial_x^2 u = f(x, t) & \text{in } (-1, 1) \times (0, T), \\ u(-1, t) = u(1, t) = \partial_x u(1, t) = 0 & \text{in } (0, T), \\ u(\cdot, 0) = u_0(\cdot) & \text{in } (-1, 1), \end{cases} \quad (1)$$

where  $u = u(x, t)$  is the state variable in  $(-1, 1) \times (0, T)$ ,  $f = f(x, t)$  is an external force acting in the system, and  $u_0$  is the initial datum. System (1) represents the so-called linear Korteweg de Vries–Burgers (KdVB) equation. In 1895, Korteweg and de Vries developed an evolutionary model to describe the propagation of long water waves in channels of shallow depth, namely, KdV equation, in which two phenomena are involved, dispersion (third-order derivative) and nonlinear convection (nonlinear term). The interaction of these terms gives rise to a wave traveling at constant speed without losing its sharp, called soliton [2, 12, 24]. As consequence of the union of the KdV and Burgers equations arise the KdVB equation, which in our case has homogeneous non-periodic boundary conditions.

From a numerical point of view, KdVB-type equations with constant coefficients have been widely studied by means of different methods; see for instance the works [31, 37, 11, 23, 27, 28] and references therein for more details.

On the other hand, by introducing variable coefficients  $\alpha(t) > 0$  and  $\beta(t) > 0$ , the KdVB equation (1) is useful to describe solitonic propagation in fluids [38], a variety of cosmic plasma phenomena [15, 26, 36, 16], among others. Motivated by those applications and as mentioned, as far as we know, an exhaustive numerical study for (1) has not been reported. Therefore, our article fill this gap giving theoretical–numerical answers to the relation between them, as well as indicating appropriate ranges where the solutions can be tested.

### 2.1. Legendre–Petrov–Galerkin method.

In this subsection we formulate a fully discrete finite element scheme based in the LPG method for solving (1). We begin by describing the LPG approximation framework and listing the basic properties used in the analysis.

For any real constants  $a, b$ , let  $\omega^{a,b}(x) = (1-x)^a(1+x)^b$  be weight functions on  $(-1, 1) =: I$ . The inner product and norm in  $L^2_{\omega^{a,b}}(I)$  are denoted by  $(\cdot, \cdot)_{\omega^{a,b}}$  and  $\|\cdot\|_{\omega^{a,b}}$  respectively. We will omit the subscript  $\omega^{a,b}$  whenever  $\omega^{a,b}(x) = 1$ . Let  $\mathbb{P}_N(I)$  be the space of polynomials of degree at most  $N$  on the interval  $I$  and

$$V_N = \mathbb{P}_N(I) \cap H_0^{2,1}(I), \quad W_N = \mathbb{P}_N(I) \cap H_0^1(I),$$

where  $H_0^{2,1}(I) = \{v \in H^2(I) \cap H_0^1(I) : \partial_x v(1) = 0\}$ .

Let  $L_k$  be the  $k$ th degree Legendre polynomial. To continuation we recall some properties of Legendre polynomials which will be used in this paper (see [34]).

$$\int_{-1}^1 L_j(x)L_k(x)dx = \frac{2}{2k+1}\delta_{jk}. \quad (2)$$

$$L_n(x) = \frac{1}{2n+1}(L'_{n+1}(x) - L'_{n-1}(x)), \quad n \in \mathbb{N}. \quad (3)$$

$$L'_n(x) = \sum_{\substack{k=0 \\ k+n \text{ odd}}}^{n-1} (2k+1)L_k(x). \quad (4)$$

Bonnet's recursion formula:

$$(2n+1)xL_n(x) = (n+1)L_{n+1}(x) + nL_{n-1}(x), \quad n \in \mathbb{N}. \quad (5)$$

Now, the semidiscrete LPG method for (1) consists in finding  $u_N(t) \in V_N$  such that for almost every  $t \in (0, T)$

$$\begin{cases} (\partial_t u_N(t), v) + \alpha(t)(\partial_x^3 u_N(t), v) - \beta(t)(\partial_x^2 u_N(t), v) = (f(t), v) & \forall v \in W_{N-1}, \\ (u_N(0), v) = (u_0, v) & \forall v \in W_{N-1}, \end{cases} \quad (6)$$

holds.

From [27], we shall use appropriate basis functions such that the corresponding matrices are sparse. To this end, for  $N \geq 3$  and  $n = [0, N-3]$ , we define the basis functions  $\{\phi_n\}$  for the space  $W_{N-1}$  by:

$$\phi_n(x) = c_{n+1}(L_n(x) - L_{n+2}(x)), \quad c_n = \frac{1}{2n+1}.$$

By taking into account (3), it is easy to verify that  $\partial_x \phi(x) = -L_{n+1}(x)$ .

Next, we introduce the semidiscrete state variable  $u_N(\cdot, t) \in V_N$  on spectral space and its vector representation:

$$u_N(\cdot, t) = (1-x) \sum_{n=0}^{N-3} \hat{u}_n(t) \phi_n(\cdot), \quad \mathbf{u}(t) = (\hat{u}_0(t), \dots, \hat{u}_{N-3}(t))^T.$$

Respect to the time discretization, a classical forward scheme is considered. Thus, let  $\Delta t$  be the step size in time space and  $t_k = k\Delta t$  ( $k = \overline{[0, n_T]}$ ) and  $t_{N_T} = T = n_T \Delta t$ .

By simplicity,  $v^k(x) := v(x, t_k)$  is denoted by  $v^k$  and

$$v^{k+\frac{1}{2}} = \frac{1}{2}(v^{k+1} + v^k).$$

The fully discrete spectral method for (1) reads: to find  $u_N^k \in V_N$  such that

$$\begin{cases} (\Delta t)^{-1}(u_N^{k+1} - u_N^k, v) + \alpha(t_k)(\partial_x^3 u_N^{k+\frac{1}{2}}, v) - \beta(t_k)(\partial_x^2 u_N^{k+\frac{1}{2}}, v) = (f^{k+\frac{1}{2}}, v) & \forall v \in W_{N-1}, \\ (u_N^0, v) = (u_0, v) & \forall v \in W_{N-1}, \end{cases} \quad (7)$$

for  $k = \overline{[0, n_T - 1]}$ .

## 2.2. Stability analysis.

In this subsection we establish the stability of the Legendre–Petrov Galerkin method for solving the discrete system (7). Before that, some theoretical properties in weighted spaces must be considered.

The following lemma establishes a Poincaré–type inequality [33].

**Lemma 2.1.** *Let  $u \in V_N$ . Then,*

$$\int_I \frac{|u(x)|^2}{(1-x)^3} dx \leq \int_I \frac{|\partial_x u(x)|^2}{1-x} dx.$$

**Remark 2.1.** *Observe that, for any  $v \in W_{N-1}$  and  $u \in V_N$  follows*

$$-(\partial_x^2((1-x)v), \partial_x v) = 2\|\partial_x v\|^2 - ((1-x)\partial_x^2 v, \partial_x v) = \frac{3}{2}\|\partial_x v\|^2 + |\partial_x v(-1)|^2$$

and

$$-(\partial_x^2 u, (1-x)^{-1}u) = ((1-x)^{-2}u, \partial_x u) + ((1-x)^{-1}\partial_x u, \partial_x u) = -\|u\|_{\omega^{-3,0}}^2 + \|\partial_x u\|_{\omega^{-1,0}}^2 \geq 0,$$

where the above inequality is consequence of Lemma 2.1.

The next theorem provides expressions for the stability of the LPG scheme given in (7).

**Theorem 2.1.** *Let  $T > 0$  and  $\omega(x) = \omega^{-1,0}(x)$ . Then,*

i) *Assume  $\beta(t) \geq 0$  and  $\alpha(t) \geq \frac{1}{3\ell}$ , for any  $\ell \geq 1$  and  $0 \leq t \leq T$ . Then, the LPG approximation  $u_N^k$  of (1) satisfies*

$$\begin{aligned} & \|u_N^n\|_{\omega}^2 + \Delta t \sum_{k=0}^{n-1} (3\ell\alpha(t_k) - 1) \|\partial_x u_N^{k+\frac{1}{2}}\|^2 + \Delta t \sum_{k=0}^{n-1} \alpha(t_k) |u_N^{k+\frac{1}{2}}(-1)|^2 \\ & \quad + \Delta t \sum_{k=0}^{n-1} \beta(t_k) (\|\partial_x u_N^{k+\frac{1}{2}}\|_{\omega}^2 - \|u_N^{k+\frac{1}{2}}\|_{\omega^{-3,0}}^2) \\ & \leq 8\ell \|u_N^0\|_{\omega}^2 + 8\Delta t \ell^2 \sum_{k=0}^{n-1} \|f^{k+\frac{1}{2}}\|_{H^{-1}(I)}^2, \end{aligned} \quad (8)$$

for all  $0 < n \leq n_T$ .

ii) Assume  $\beta(t) > 0$  and  $\alpha(t) > 0$ , for  $t \in [0, T]$ . Then, the LPG approximation  $u_N^k$  of (1) satisfies

$$\begin{aligned} & \|u_N^n\|_\omega^2 + \Delta t \sum_{k=0}^{n-1} \alpha(t_k) \|\partial_x u_N^{k+\frac{1}{2}}\|^2 + \Delta t \sum_{k=0}^{n-1} \alpha(t_k) |u_N^{k+\frac{1}{2}}(-1)|^2 \\ & \quad + \Delta t \sum_{k=0}^{n-1} \beta(t_k) (\|\partial_x u_N^{k+\frac{1}{2}}\|_\omega^2 - \|u_N^{k+\frac{1}{2}}\|_{\omega^{-3,0}}^2) \\ & \leq 4\|u_N^0\|_\omega^2 + 4\Delta t \sum_{k=0}^{n-1} \frac{1}{\alpha(t_k)} \|f^{k+\frac{1}{2}}\|_{H^{-1}(I)}^2, \end{aligned} \quad (9)$$

for all  $0 < n \leq n_T$ .

*Proof of Theorem 2.1.*

i) Let us consider the test function  $v = 2\ell v_N^{k+\frac{1}{2}}$  in (7), with  $v_N^k = u_N^k \omega$ . Then, after using remark 2.1 we get

$$\begin{aligned} & 2\ell(\Delta t)^{-1}(u_N^{k+1} - u_N^k, u_N^k \omega) + 3\ell\alpha(t_k) \|\partial_x v^{k+\frac{1}{2}}\|^2 + 2\ell\alpha(t_k) |\partial_x v^{k+\frac{1}{2}}(-1)|^2 \\ & \quad + 2\ell\beta(t_k) (-\|u_N^{k+\frac{1}{2}}\|_{\omega^{-3,0}}^2 + \|\partial_x u_N^{k+\frac{1}{2}}\|_\omega^2) \\ & \leq 2|(f^{k+\frac{1}{2}}, \ell v_N^{k+\frac{1}{2}})|. \end{aligned} \quad (10)$$

Using the fact that  $\|u\|_{H^{-1}(I)} = \sup_{v \in H_0^1(I)} \frac{|(u,v)|}{|v|_2}$  and Young's inequality (i.e.,  $ab \leq \frac{a^p}{p} + \frac{b^q}{q}$ ;  $\frac{1}{p} + \frac{1}{q} = 1$ ;  $a, b \geq 0$ ) with  $p = q = 2$  and  $a = \ell|f^{k+\frac{1}{2}}|$ ,  $b = |v_N^{k+\frac{1}{2}}|$ , the right hand side of the previous estimate can be estimated by

$$2|(f^{k+\frac{1}{2}}, \ell v_N^{k+\frac{1}{2}})| \leq \ell^2 \|f^{k+\frac{1}{2}}\|_{H^{-1}(I)}^2 + \|\partial_x v_N^{k+\frac{1}{2}}\|^2.$$

Replacing the above estimate into (10) and summing for  $k = \overline{[0, n-1]}$ , we obtain

$$\begin{aligned} & \ell \|u_N^n\|_\omega^2 + \Delta t \sum_{k=0}^{n-1} (3\ell\alpha(t_k) - 1) \|\partial_x v_N^{k+\frac{1}{2}}\|^2 + 2\Delta t \ell \sum_{k=0}^{n-1} \alpha(t_k) |v_N^{k+\frac{1}{2}}(-1)|^2 \\ & \quad + 2\Delta t \ell \sum_{k=0}^{n-1} \beta(t_k) (-\|u_N^{k+\frac{1}{2}}\|_{\omega^{-3,0}}^2 + \|\partial_x u_N^{k+\frac{1}{2}}\|_\omega^2) \\ & \leq \ell \|u_N^0\|_\omega^2 + \Delta t \ell^2 \sum_{k=0}^{n-1} \|f^{k+\frac{1}{2}}\|_{H^{-1}(I)}^2, \end{aligned}$$

Finally, note that  $\partial_x u_N^{k+\frac{1}{2}}(-1) = 2\partial_x v_N^{k+\frac{1}{2}}(-1)$  and

$$\|\partial_x u_N^{k+\frac{1}{2}}\|^2 \leq 2\|(1-x)\partial_x v_N^{k+\frac{1}{2}}\|^2 + 2\|\partial_x v_N^{k+\frac{1}{2}}\|^2 \leq 8\|\partial_x v_N^{k+\frac{1}{2}}\|^2.$$

This argument allows to deduce (8) and ends the proof to the first case.

ii) Since the proof of (9) follows the above structure, we have omitted the details. However, in this case, the term  $(f^{k+\frac{1}{2}}, v_N^{k+\frac{1}{2}})$  is upper bounded by using Young's inequality (i.e.,  $ab \leq \frac{a^p}{p} + \frac{b^q}{q}$ ;  $\frac{1}{p} + \frac{1}{q} = 1$ ;  $a, b \geq 0$ ) with  $p = q = 2$  and  $a = \alpha^{\frac{1}{2}}|v_N^{k+\frac{1}{2}}|$ ,  $b = \alpha^{-\frac{1}{2}}|f^{k+\frac{1}{2}}|$ .

This concludes the proof of Theorem 2.1.  $\square$

**Remark 2.2.** In the dissipative case (that is,  $\alpha = 0$ ) where the symmetry of the main operator is guaranteed, a Galerkin approximation with Legendre polynomials in  $W_N$  turns out to be more convenient than the Petrov–Galerkin method. Otherwise, a LPG scheme might be unstable even for certain constant dissipation coefficients.

**Remark 2.3.** Theorem 2.1 allows to visualize how the presence of a positive time–dependent dispersion coefficient could affect the stability if an external source acts into the system, see (9). Nevertheless, it can be corrected by considering a restriction upon the dispersion coefficient, and therefore the LPG method is stable, see (8).

### 2.3. Error analysis

In this paragraph, we present approximation properties of some projection operators, which are used later on. First, we recall a basic result of Jacobi polynomial approximation [25]. Let  $P_N^{a,b}$  be the  $L^2_{\omega^{a,b}}(I)$ -orthogonal projector  $L^2_{\omega^{a,b}}(I) \mapsto \mathbb{P}_N(I)$  and by simplicity,  $P_N := P_N^{0,0}$ .

**Lemma 2.2.** *Assume  $a, b > 1$  and  $r > 0$ . Then, for any  $v \in H^r(I)$  and any  $0 \leq s \leq r$ ,*

$$\|\partial_x^s(P_N^{a,b}v - v)\|_{\omega^{a+s,b+s}} \leq CN^{s-r}\|\partial_x^r v\|_{\omega^{a+r,b+r}}. \quad (11)$$

Now, from [27], we define  $\Pi_N : H_0^{2,1}(I) \mapsto V_N$  such that

$$(\partial_x^2(\Pi_N u - u), \partial_x v) = 0, \quad \forall v \in W_{N-1}. \quad (12)$$

Moreover,  $\Pi_N$  satisfies

$$\Pi_N u := \bar{\partial}_x^{-2} P_{N-2} \partial_x^2 u, \quad (13)$$

where

$$\bar{\partial}_x^{-1} v(x) := - \int_x^1 v(y) dy, \quad \bar{\partial}_x^{-i} v(x) = (\bar{\partial}_x^{-1})^i v(x).$$

**Lemma 2.3.** *Assume  $u \in H_0^{2,1}(I) \cap H^r(I)$  and  $r \geq 2$ . Then*

- i)  $\|\partial_x^s(\Pi_N u - u)\|_{\omega^{s-2,s-2}} \leq CN^{s-r}\|\partial_x^r u\|_{\omega^{r-2,r-2}}$ , for any  $0 \leq s \leq 2$ .
- ii)  $(\Pi_N u - u, v) = 0$ , for all  $v \in \mathbb{P}_{N-4}(I)$ .
- iii)  $\|\partial_x(\Pi_N u - u)\| \leq CN^{2-r}\|\partial_x^r u\|_{\omega^{r-2,r-2}}$ .

*Proof.* The proof of the first two items can be found in [25]. Thus, we only proof the last point.

Then, using Lemma 2.2, (13), the first part of this lemma, and also the Poincaré inequality, we can deduce

$$\begin{aligned} \|\partial_x(\Pi_N u - u)\|^2 &= (\partial_x(\Pi_N u - u), \partial_x \bar{\partial}_x^{-1}(\partial_x(\Pi_N u - u))) \\ &= |(\partial_x^2(\Pi_N u - u), \bar{\partial}_x^{-1}(\partial_x(\Pi_N u - u)))| \\ &= |((P_{N-2} - I)\partial_x^2 u, \bar{\partial}_x^{-1}(\partial_x(\Pi_N u - u)))| \\ &= |((P_{N-2} - I)\partial_x^2 u, \Pi_N u - u)| \\ &\leq \|(P_{N-2} - I)\partial_x^2 u\| \|\Pi_N u - u\| \\ &\leq CN^{2-r}\|\partial_x^r u\|_{\omega^{r-2,r-2}} \|\partial_x(\Pi_N u - u)\|. \end{aligned}$$

□

Now, for the error analysis, let  $u_N^k$  be the numerical solution of the scheme (7) and let  $u \in X$  be a solution associated to (1), where

$$X \equiv C([0, T]; H_0^{2,1}(I) \cap H^r(I)) \cap H^1(0, T; H_0^{2,1}(I) \cap H^{\max\{2, r-1\}}(I)) \cap H^3(0, T; H^{-1}(I)), \quad r \geq 2.$$

Moreover, an assumption on the coefficients  $\alpha, \beta \in L^\infty([0, T])$  must be imposed, namely:

**H1.** For every  $\varepsilon_1, \varepsilon_2 > 0$ ,

$$\left( \left( \frac{3}{8} - \frac{1}{16} \varepsilon_1 \right) \alpha^k - \left( \frac{1}{8} \varepsilon_2 + \frac{9}{8} \right) \beta^k \right) > 0, \quad \forall k = \overline{[0, n_T - 1]}. \quad (14)$$

In what follows,  $\hat{e}_N^k = \Pi_N u(\cdot, t_k) - u_N^k$ ,  $\tilde{e}_N^k = u(\cdot, t_k) - \Pi_N u(\cdot, t_k)$ , and  $e_N^k = u(\cdot, t_k) - u_N^k = \tilde{e}_N^k + \hat{e}_N^k$ .

**Theorem 2.2.** *Let  $u \in X$  and let H1 be satisfied. Then, for  $0 \leq n \leq n_T$*

$$\|u_N^n - u^n\| \leq \sqrt{2} \|u_N^n - u^n\|_{\omega^{-1,0}} \lesssim C_\alpha (N^{-r} + (\Delta t)^2) + C_\beta (N^{1-r} + (\Delta t)^2), \quad (15)$$

where  $C_\alpha \approx \left( \min_{t \in [0, T]} \alpha(t) \right)^{-1}$  and  $C_\beta \approx \|\beta\|_{L^\infty([0, T])}$ .

*Proof of Theorem 2.2.* From (1), (7) and (12), for  $k = \overline{[0, n_T - 1]}$  and for any  $v \in W_{N-1}$  we get

$$\begin{cases} (\Delta t)^{-1}(\hat{e}_N^{k+1} - \hat{e}_N^k, v) - \alpha^k(\partial_x^2 \hat{e}_N^{k+\frac{1}{2}}, \partial_x v) - \beta^k(\partial_x^2 \hat{e}_N^{k+\frac{1}{2}}, v) = (g^k, v) + \beta^k(\partial_x^2 \hat{e}_N^{k+\frac{1}{2}}, v) - \beta^k(\partial_x^2 e_N^{k+\frac{1}{2}}, v), \\ (\hat{e}_N^0, v) = (\Pi_N u^0 - u_N^0, v), \end{cases}$$

where

$$g^k = \partial_t u^{k+\frac{1}{2}} - \Pi_N \partial_t u^k.$$

By simplicity, let  $\omega(x) = \omega^{-1,0}(x)$ . Considering in the previous system the test function  $v = 2\omega \hat{e}_N^{k+\frac{1}{2}}$ , and using Remark 2.1, we get

$$\begin{aligned} & (\Delta t)^{-1}(\|\hat{e}_N^{k+1}\|_\omega^2 - \|\hat{e}_N^k\|_\omega^2) + 3\alpha^k \|\partial_x(\omega \hat{e}_N^{k+\frac{1}{2}})\|^2 + 2\alpha^k |\partial_x(\omega \hat{e}_N^{k+\frac{1}{2}})(-1)|^2 \\ & \quad + 2\beta^k (-\|\hat{e}_N^{k+\frac{1}{2}}\|_{\omega^{-3,0}}^2 + \|\partial_x \hat{e}_N^{k+\frac{1}{2}}\|_\omega^2) \\ & = 2(g^k, \omega \hat{e}_N^{k+\frac{1}{2}}) + 2\beta^k (\partial_x^2 \hat{e}_N^{k+\frac{1}{2}}, \omega \hat{e}_N^{k+\frac{1}{2}}) + 2\beta^k (\partial_x e_N^{k+\frac{1}{2}}, \partial_x(\omega \hat{e}_N^{k+\frac{1}{2}})). \end{aligned} \quad (16)$$

From Lemma 2.2, Lemma 2.3 and Young's inequality (i.e,  $ab \leq \frac{a^2}{2\varepsilon} + \frac{\varepsilon b^2}{2}$ ,  $\varepsilon > 0$ ) follows:

$$\begin{aligned} |(g^k, \omega \hat{e}_N^{k+\frac{1}{2}})| & \leq |(\partial_t u^{k+\frac{1}{2}} - \partial_t u^k, \omega \hat{e}_N^{k+\frac{1}{2}})| + |((I - \Pi_N)\partial_t u^k, (I - P_{N-4})\omega \hat{e}_N^{k+\frac{1}{2}})| \\ & \leq C(\|\partial_t u^{k+\frac{1}{2}} - \partial_t u^k\|_{H^{-1}(I)} + N^{-r}\|\partial_t u^k\|_{H^{\max(2,r-1)}(I)})\|\partial_x(\omega \hat{e}_N^{k+\frac{1}{2}})\| \\ & \leq \frac{\varepsilon_1 \alpha^k}{2} \|\partial_x(\omega \hat{e}_N^{k+\frac{1}{2}})\|^2 + C_{\alpha^k, \varepsilon_1} (\|\partial_t u^{k+\frac{1}{2}} - \partial_t u^k\|_{H^{-1}(I)}^2 + N^{-2r}\|\partial_t u^k\|_{H^{\max(2,r-1)}(I)}^2), \end{aligned}$$

where  $C_{\alpha^k, \varepsilon_1} = \frac{C^2}{2\varepsilon_1 \alpha^k}$ , for every  $\varepsilon_1 > 0$ .

Observe that the last two terms in the right-hand side of (16) can be upper bounded by using again Young's inequalities. Thus, putting together those estimates, we obtain

$$\begin{aligned} & (\Delta t)^{-1}(\|\hat{e}_N^{k+1}\|_\omega^2 - \|\hat{e}_N^k\|_\omega^2) + 3\alpha^k \|\partial_x(\omega \hat{e}_N^{k+\frac{1}{2}})\|^2 + 2\alpha^k |\partial_x(\omega \hat{e}_N^{k+\frac{1}{2}})(-1)|^2 \\ & \quad + 2\beta^k (-\|\hat{e}_N^{k+\frac{1}{2}}\|_{\omega^{-3,0}}^2 + \|\partial_x \hat{e}_N^{k+\frac{1}{2}}\|_\omega^2) \\ & \leq \frac{\varepsilon_1 \alpha^k}{2} \|\partial_x(\omega \hat{e}_N^{k+\frac{1}{2}})\|^2 + C_{\alpha^k, \varepsilon_1} (\|\partial_t u^{k+\frac{1}{2}} - \partial_t u^k\|_{H^{-1}(I)}^2 + N^{-2r}\|\partial_t u^k\|_{H^{\max(2,r-1)}(I)}^2) \\ & \quad + \varepsilon_2 \beta^k \|\partial_x(\omega \hat{e}_N^{k+\frac{1}{2}})\|^2 + \frac{\beta^k}{\varepsilon_2} \|\partial_x \hat{e}_N^{k+\frac{1}{2}}\|^2 + \beta^k \|\partial_x e_N^{k+\frac{1}{2}}\|^2 + \beta^k \|\partial_x(\omega \hat{e}_N^{k+\frac{1}{2}})\|^2, \end{aligned} \quad (17)$$

for every  $\varepsilon_1, \varepsilon_2 > 0$ .

Thus, assuming the relation

$$\left( \left(3 - \frac{1}{2}\varepsilon_1\right)\alpha^k - (\varepsilon_2 + 1)\beta^k \right) > 0$$

and adding for  $k = \overline{[0, n_T - 1]}$ , we deduce

$$\begin{aligned} & \|\hat{e}_N^n\|_\omega^2 + \Delta t \sum_{k=0}^{n_T-1} \left( \left(3 - \frac{1}{2}\varepsilon_1\right)\alpha^k - (\varepsilon_2 + 1)\beta^k \right) \|\partial_x(\omega \hat{e}_N^{k+\frac{1}{2}})\|^2 \\ & \quad + 2\Delta t \sum_{k=0}^{n_T-1} \beta^k (-\|\hat{e}_N^{k+\frac{1}{2}}\|_{\omega^{-3,0}}^2 + \|\partial_x \hat{e}_N^{k+\frac{1}{2}}\|_\omega^2) \\ & \leq \|\hat{e}_N^0\|_\omega^2 + \Delta t \sum_{k=0}^{n_T-1} \frac{\beta^k}{\varepsilon_2} \|\partial_x \hat{e}_N^{k+\frac{1}{2}}\|^2 + \beta^k \|\partial_x e_N^{k+\frac{1}{2}}\|^2 \\ & \quad + \Delta t \sum_{k=0}^{n_T-1} C_{\alpha^k, \varepsilon_1} (\|\partial_t u^{k+\frac{1}{2}} - \partial_t u^k\|_{H^{-1}(I)}^2 + N^{-2r}\|\partial_t u^k\|_{H^{\max(2,r-1)}(I)}^2), \end{aligned}$$

for every  $\varepsilon_1, \varepsilon_2 > 0$ .

Now, using the hypothesis H1 and from the fact that

$$\|\partial_x e_N^{k+\frac{1}{2}}\|^2 \leq 2\|(1-x)\partial_x(\omega \hat{e}_N^{k+\frac{1}{2}})\|^2 + 2\|\partial_x(\omega e_N^{k+\frac{1}{2}})\|^2 \leq 8\|\partial_x(\omega \hat{e}_N^{k+\frac{1}{2}})\|^2,$$

the above inequality can be transformed by:

$$\begin{aligned}
& \|\hat{e}_N^n\|_\omega^2 + \Delta t \sum_{k=0}^{n_T-1} \left( \left( \frac{3}{8} - \frac{1}{16} \varepsilon_1 \right) \alpha^k - \left( \frac{1}{8} \varepsilon_2 + \frac{9}{8} \right) \beta^k \right) \|\partial_x e_N^{k+\frac{1}{2}}\|^2 \\
& \quad + 2\Delta t \sum_{k=0}^{n_T-1} \beta^k \left( -\|\hat{e}_N^{k+\frac{1}{2}}\|_{\omega^{-3,0}}^2 + \|\partial_x \hat{e}_N^{k+\frac{1}{2}}\|_\omega^2 \right) \\
& \leq \|\hat{e}_N^0\|_\omega^2 + \varepsilon_2^{-1} \|\beta\|_{L^\infty([0,T])} \Delta t \sum_{k=0}^{n_T-1} \|\partial_x \hat{e}_N^{k+\frac{1}{2}}\|^2 \\
& \quad + C\varepsilon_1^{-1} \left( \min_{t \in [0,T]} \alpha(t) \right)^{-1} \Delta t \sum_{k=0}^{n_T-1} \left( \|\partial_t u^{k+\frac{1}{2}} - \partial_t u^k\|_{H^{-1}(I)}^2 + N^{-2r} \|\partial_t u^k\|_{H^{\max(2,r-1)}(I)}^2 \right),
\end{aligned} \tag{18}$$

for every  $\varepsilon_1, \varepsilon_2 > 0$ .

Finally, we estimate the terms in the right-hand side of (18). To do that, we use Lemma 2.3 and [25]. Then, a direct computation allows us to obtain the inequalities:

$$\begin{aligned}
& \Delta t \sum_{k=0}^{n-1} \|\partial_t u^{k+\frac{1}{2}} - \partial_t u^k\|_{H^{-1}(I)}^2 \leq C(\Delta t)^4 \|\partial_t^3 u\|_{L^2(0,T;H^{-1}(I))}^2, \\
& \Delta t \sum_{k=0}^{n-1} \|\partial_t u^k\|_{H^{\max(2,r-1)}(I)}^2 \leq C \|\partial_t u\|_{L^2(0,T;H^{\max(2,r-1)}(I))}^2, \\
& \sum_{k=0}^{n_T-1} \|\partial_x \hat{e}_N^{k+\frac{1}{2}}\|^2 \leq CN^{2(1-r)} \|\partial_x^r u\|_{\omega^{r-2,r-2}}^2, \quad \forall r \geq 2 \quad \text{and} \quad \|\tilde{e}^0\|_\omega \leq CN^{-r} \|u_0\|_{H^r(I)}.
\end{aligned}$$

Therefore, using the above estimates and the triangular inequality in (18), the desired inequality is obtained. This arguments complete the proof of Theorem 2.2.  $\square$

**Remark 2.4.** *It is worth mentioning that the convergence analysis only for the KdV equation with the same method was done in [27] for constant coefficients, that means, in (1)  $\alpha(t) = 1$  and  $\beta(t) = 0$ , for  $t \in (0, T)$ . Obviously, estimate (15) implies the case proven in [27]. On the other hand, by using dual–Petrov–Galerkin bases, [33, Theorem 2.2] involves a second–order term with constant coefficient  $\beta$  in the range  $(-\frac{1}{3}, \frac{1}{6})$ , and  $\alpha = 1$ . Note that our hypothesis H1 satisfies such parameter configuration when, for instance,  $\varepsilon_1, \varepsilon_2$  go to zero.*

#### 2.4. Implementation scheme.

In this paragraph we discuss the numerically implementation of the fully discrete spectral method given in (7). We need to solve at each time level the problem of finding  $u_N^k \in V_N$  verifying

$$(u_N^{k+1}, v) + \frac{\Delta t}{2} \alpha(k\Delta t) (\partial_x^3 u_N^{k+1}, v) - \frac{\Delta t}{2} \beta(k\Delta t) (\partial_x^2 u_N^{k+1}, v) = (g^k, v) \quad \forall v \in W_{N-1}, \tag{19}$$

where

$$g^k = u_N^k - \frac{\Delta t}{2} \alpha(k\Delta t) \partial_x^3 u_N^k + \frac{\Delta t}{2} \beta(k\Delta t) \partial_x^2 u_N^k + \Delta t f^{k+\frac{1}{2}}.$$

Therefore, by considering  $u_N^k(x) = (1-x) \sum_{n=0}^{N-3} \hat{u}_n^k \phi_n(x)$  and taking as test function  $v = \phi_m$ , for  $m = \overline{[0, N-3]}$ , the above identity can be written by

$$\begin{aligned}
& \sum_{n=0}^{N-3} \left( ((1-x)\phi_n, \phi_m) + \Delta t \alpha(k\Delta t) (L_{n+1}, L_{m+1}) - \frac{\Delta t}{2} \alpha(k\Delta t) ((1-x)L_{m+1}, \partial_x L_{n+1}) \right) \hat{u}_n^{k+1} \\
& \quad + \frac{\Delta t}{2} \beta(k\Delta t) \sum_{n=0}^{N-3} \left( ((1-x)L_{n+1}, L_{m+1}) + (L_n - L_{n+2}, L_{m+1}) \right) \hat{u}_n^{k+1} \\
& = \sum_{n=0}^{N-3} (RHS)_n \hat{u}_n^k + \Delta t \sum_{n=0}^{N-3} ((1-x)\phi_n, \phi_m) f_n^{k+\frac{1}{2}},
\end{aligned}$$



where  $(RHS)_n$  corresponds to

$$(RHS)_n = ((1-x)\phi_n, \phi_m) - \Delta t \alpha(k\Delta t)(L_{n+1}, L_{m+1}) + \frac{\Delta t}{2} \alpha(k\Delta t)((1-x)L_{m+1}, \partial_x L_{n+1}) - \frac{\Delta t}{2} \beta(k\Delta t)((1-x)L_{n+1}, L_{m+1}) - \frac{\Delta t}{2} \beta(k\Delta t)(L_n - L_{n+2}, L_{m+1}).$$

Based on the above representation, we build the matrices  $K, L, M$  and  $Q$  of size  $(N-2) \times (N-2)$  with the coefficients  $k_{mn}, \ell_{mn}, a_{mn}$  and  $q_{mn}$  defined as follows:

$$k_{mn} = ((1-x)L_{n+1}, L_{m+1}) + (L_n - L_{n+2}, L_{m+1}) = \begin{cases} 2c_{m+1} & m = n, \\ 2c_m - 2(m+1)c_m c_{m+1} & n = m+1, \\ -2(1+(m+2)c_{m+1})c_{m+2} & n = m-1, \\ 0 & n \leq m-2, \\ 0 & n \geq m+2. \end{cases}$$

$$a_{mn} = ((1-x)\phi_n, \phi_m) = \begin{cases} 2c_{m+1}^2(c_m + c_{m+2}) & m = n, \\ -2c_{m+1}c_{m+2}^2(c_m + (m+3)c_{m+3}) & n = m+1, \\ -2c_{m+1}c_{m+2}c_{m+3} & n = m+2, \\ 2(m+3)c_{m+1}c_{m+2}c_{m+3}c_{m+4} & n = m+3, \\ 0 & n \geq m+4. \end{cases}$$

$$q_{mn} = ((1-x)L_{m+1}, \partial_x L_{n+1}) = \begin{cases} c_{m+1} - 1 & m = n, \\ 2(-1)^{m+n+1} & n \geq m+1, \\ 0 & n \leq m-1 \end{cases}$$

and

$$\ell_{mn} = (L_{n+1}, L_{m+1}) = \text{diag}(2C_{m+1}).$$

Therefore, the matrix representation of problem (7) is

$$\mathbf{A}\mathbf{U}^{k+1} = \mathbf{B}\mathbf{U}^k + \mathbf{C}\mathbf{F}^{k+\frac{1}{2}}, \quad (20)$$

with

$$\mathbf{A} = M + \Delta t \alpha(k\Delta t)L - \frac{\Delta t}{2} \alpha(k\Delta t)Q + \frac{\Delta t}{2} \beta(k\Delta t)K, \quad (21)$$

and

$$\mathbf{B} = M - \Delta t \alpha(k\Delta t)L + \frac{\Delta t}{2} \alpha(k\Delta t)Q - \frac{\Delta t}{2} \beta(k\Delta t)K, \quad \mathbf{C} = \Delta t M. \quad (22)$$

**Remark 2.5.** Since our approach is based in [27], the above mass matrix  $\{a_{mn}\}$  is the same, as well as a part of the term  $g^k$  given in (19). However, in [27] there are some typos and incomplete information related to implementation that we have corrected in the present work.

In order to display the stability property for the fully discrete scheme (19), in Figure 1 we plot the eigenvalues for the LPG discretization for two parametric configurations of  $\alpha$  and  $\beta$ . In relation to [27] where the stability analysis was done only for the KdV equation with  $\alpha = 1$ , we observe that for the KdVB equation with time dependent coefficients does not exist instable modes, neither. Nevertheless, as mentioned in Remark 2.2, it is possible if the constrains upon the dispersion–dissipation parameters established in Theorem 2.1 are verified. Indeed, the case where  $\alpha$  is small enough (tends to zero) leads to instables modes for small values of  $\beta$  and therefore, it is cannot be considered under this setting. Additionally, Figure 1 allow us to visualize the effect caused by the interaction among dispersion and dissipation parameters in the eigenvalues distribution of the spectral approximation.

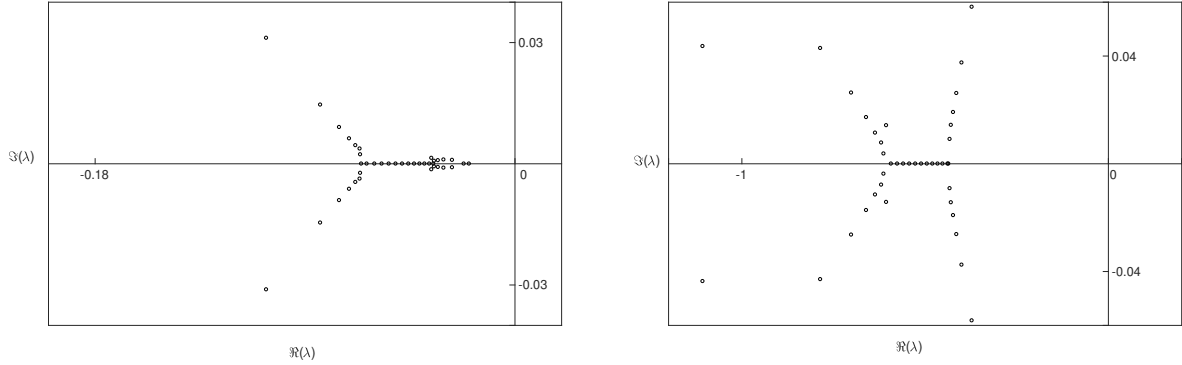


Figure 1: Eigenvalues distribution of the spectral approximation for the KdVB equation, associated to the scheme (19) and matrix (21). In both cases  $N = 42$ ,  $\Delta t = 1$ , and parameters (Left)  $\alpha = 0.1, \beta = 0.1$ , (Right)  $\alpha = 1, \beta = 0.3$ .

### 3. Numerical Results

In this section, we present results obtained from simulations of the LPG method for the KdVB equation with dispersion–diffusion variable coefficients, see (1). Recall that aspects related to stability and convergence have been previously studied in Theorem 2.1 and Theorem 2.2. In fact, those results depend on, at least, four parameters, namely,  $N$ ,  $\Delta t$ ,  $\alpha$  and  $\beta$ . In order to seek the behaviors associated to the theoretical descriptions and to separate the effects of each corresponding parameter, it is necessary to split the numerical problem in several experiments with different interactions of the aforementioned parameters. Indeed, we provide a proper calibration for the dispersion and diffusion parameters, which in turn shows numerical evidences to particular cases presented in previous works.

#### 3.1. Experimental setup

In all the cases tested, we try to set a benchmark that allow to measure every numerical experiment in a unique from. To be more exact, by considering that several variables are involved into the analysis, makes it necessary to introduce a fair measure which would be able to give precise information of the accuracy of the experiment. It is with this aim that we define the following functions, which satisfy (1). Henceforth, the initial distribution is defined by

$$u(x, 0) = \sin^2(ax) \sin(bx) \quad (23)$$

and the source term as follows:

$$\begin{aligned} f(x, t) = & \left( (c - b^3 \alpha(t)) \sin^2(ax) + 6a^2 b \alpha(t) \cos(2ax) \right) \cos(bx + ct) \\ & - a \alpha(t) (4a^2 + 3b^2) \sin(2ax) \sin(bx + ct) \\ & + \beta(t) \left( -(2a^2 \cos(2ax) - b^2 \sin^2(ax)) \sin(bx + ct) - 2ab \sin(2ax) \cos(bx + ct) \right), \end{aligned} \quad (24)$$

where  $a = \pi$  and  $b = c = 12$ .

Taking into account the above data, the unique solution to (1) can be obtained analytically. In fact, the explicit form of the solution is given by

$$u(x, t) = \sin^2(ax) \sin(bx + ct). \quad (25)$$

Note that the source (24) really corresponds to a biparametric family, although its associated solution (25) is free of parameters. In other words, all information concerning to the dispersion–dissipation parameters is located in the source instead of the solution, which allow us to create uniformly measurement errors respect to the analytical solution. Therefore, we define the error  $\epsilon$  in the norms  $L^p$  ( $1 \leq p < \infty$ ) in space and  $L^1$  in time as follows:

$$\epsilon := \frac{\Delta t}{N} \sum_{k=0}^{n_T} \left( \sum_{j=0}^N |u(x_j, t_k) - u_N^k(x_j)|^p \right)^{1/p}. \quad (26)$$

On the other hand, it is worth pointing out that the values of  $a, b$  and  $c$  have been taken from [27], where the authors defined (23)–(25) for the KdV equation with dispersion coefficient  $\alpha = 1$ .

Here,  $x_j$  represents the specific position defined by the Chebyshev–Gauss–Lobatto points [4], whereas  $t_k$  is the temporal discretization defined in the previous section. Clearly, our work constitutes an extension to the linear model given in [27].

### 3.2. Temporal and spatial discretization

The main task in this paragraph consists on providing evidence according to Theorem 2.2. Since the spatial and temporal approximations show rate of convergence linked to the dispersion and diffusion parameters, we pretend to observe both tendencies throughout the same numerical experiment defined by (23)–(25), but using different parametric configurations depending on the case.

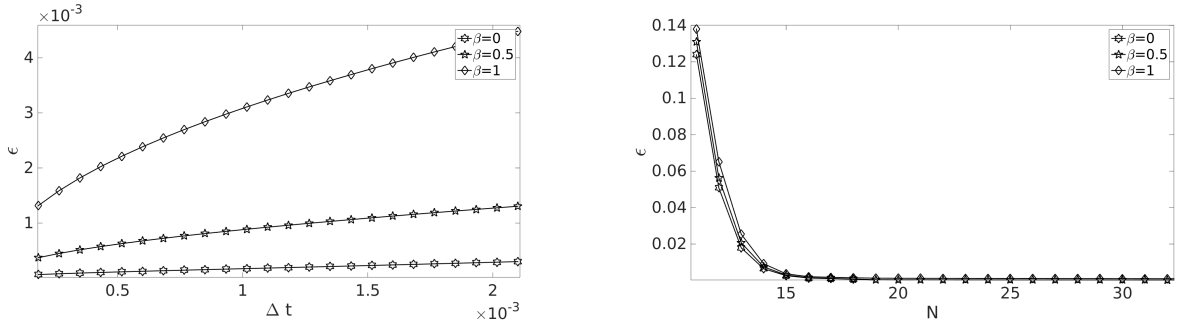


Figure 2: Each mark corresponds to the error  $\epsilon$  in  $L^1(L^2)$ -norm for  $\alpha = 1$  and three different  $\beta$  values. (Left) temporal convergence and (Right) spatial convergence.

Table 1: Analysis of the temporal convergence using least squares method, and fitting the solution of the numerical problem by  $u_N^k = u(x_n, t_k)[1 + (\Delta t)^{\text{order}}]$ . In all simulations we fix  $\alpha = 1$  and  $N = 32$ . Here, the extrapolated error values using (26) with  $p = 1$  and  $p = 2$  as well as their corresponding convergence orders are recorded.

$\beta$	$L^1(L^1)$ – norm	order	$L^1(L^2)$ – norm	order
0	0.01335901	1.87	0.00010075	2.80
0.2	0.04785512	1.90	0.00046410	2.72
0.4	0.16367134	2.10	0.00169221	2.54
0.6	0.39841512	2.48	0.00316313	2.23
0.8	0.71474315	2.62	0.00485123	1.71

First, we focus on the temporal convergence of the method. As starting point, we develop a massive experiment fixing the number of modes and the dispersion parameter, namely,  $N = 32$  and  $\alpha = 1$ , respectively. Besides, for five different  $\beta$  values, e.g.  $\beta = \{0, 0.2, 0.4, 0.6, 0.8\}$ , we carry out 20 simulations of  $T = 2$  seconds of time by fixing steps  $\Delta t$  in the range  $\{(i+1)10^{-4} : i = 1, \dots, 20\}$ . In order to achieve a better visualization and without less of generality, we only depict three different cases of  $\beta$  values in Figure 2 (Left), where each curve represents a dispersion parameter  $\beta$  and every mark shows the error obtained upon its corresponding temporal step  $\Delta t$ . Note that, by fixing the dispersion coefficient at  $\alpha = 1$ , we clearly observe a convergence of the value of  $\epsilon$  to zero, although its rate of convergence is affected by the  $\beta$  dissipation coefficients. Motivated by this, it is interesting to study the order of convergence for each curve by using a least squares fit. Table 1 shows the five different  $\beta$  dissipation coefficients where both the order of convergence and the extrapolated error values are recorded. We can see that in average the temporal convergence tends to 2 as expected from theoretical result, see (15).

Now, the spatial convergence analysis is carried out upon the same numerical experiment but, fixing both the temporal sampling to  $\Delta t = 10^{-4}$  seconds and the dispersion parameter to  $\alpha = 1$ . Again, the  $\beta$  parameter is evaluated

Table 2: Error analysis in  $L^1(L^2)$ -norm for seven different values of  $N$  and five different values of  $\beta$ . Besides,  $\alpha = 1$  and  $\Delta t = 10^{-4}$  seconds.

$\beta$	$N = 14$	$N = 16$	$N = 18$	$N = 20$	$N = 22$	$N = 24$	$N = 26$
0	0.00645621	0.00135455	0.00066981	0.00011939	0.00015875	0.00010339	0.00008585
0.2	0.00691887	0.00140829	0.00069669	0.00018076	0.00020508	0.00016183	0.00014666
0.4	0.00764791	0.00153235	0.00081798	0.00042376	0.00038715	0.00036853	0.00035271
0.6	0.00865866	0.00183839	0.00119356	0.00091525	0.00088213	0.00083909	0.00080551
0.8	0.00983571	0.00240629	0.00185255	0.00161797	0.00155112	0.00148371	0.00142658

at  $\beta = \{0, 0.2, 0.4, 0.6, 0.8\}$  whereas, the number of nodes,  $N$ , is progressively selected in the range  $11 \leq N \leq 32$ . The results are depicted in Figure 2 (Right), where we observe a sharp accuracy convergence around  $14 \leq N \leq 22$  nodes. In fact, Figure 2 (Right) allow to deduce that the convergence order is much greater than two, it makes imposible to create any confident approximation based on least squares fitting. To precise this feature, we show in Table 2 the error values in the  $L^1(L^2)$ -norm for five different  $\beta$  values and seven different values of  $N$ . In concordance with our theoretical result on convergence, Theorem 2.2, we should note that for any value of  $N$ , the dispersive case ( $\beta = 0$ ) is always more accurate than the other choices of  $\beta$  values. In addition, it is worth mentioning that the results shown in Figure 2 (Right) and in Table 2 are not enough to establish which is exactly the convergence order,  $r$ , and the dependence of  $N$  in the accuracy of the results. Also, it is true that we observe a faster tendency in the accuracy than for the temporal convergence, but the fact that  $r$  is only bounded and cannot be fitted as a simple number, it makes necessary to broad the vision and to study the spatial convergence through other considerations always in completely agreement with the theory already exposed.

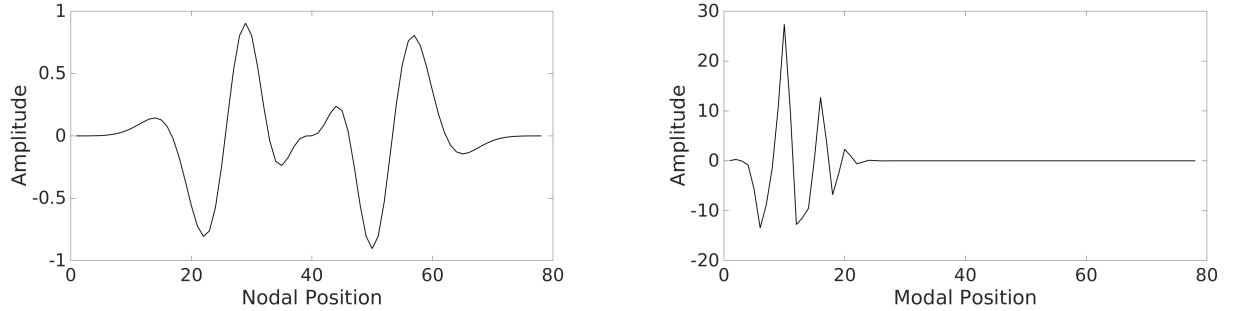


Figure 3: The numerical representation of the initial condition, (23), represented in (Left) the nodal-domain,  $u_N^0$ , and (Right) the modal-domain,  $\hat{u}_n^0$ . In both cases we use  $N = 80$ .

Considering the scheme developed in subsection 2.4, it is important to recall that our approach constitutes a global method for the space discretization and, therefore, the computed quantities are  $\hat{u}_n^k$ , and not the spatial values  $u_N^k$ . Thus, the information is obtained from the modal basis ( $\phi$ -basis), it means that all the modes of the  $\phi$ -domain influence in each spatial node defined in the mesh. Therefore, it turns out interesting to observe which form takes the signal represented in the modal basis ( $\phi$ -basis). More precisely, we focus the analysis on both, the initial condition and the source term studying the main features of their modal representation. First, we take the initial condition (23). Note that Figure 3 (Left) displays the snapshots of the signal into the nodal space,  $u_N^0$ , whereas Figure 3 (Right) represents the transformed signal into the  $\phi$ -domain,  $\hat{u}_n^0$ . The most interesting feature appears when on the right-hand side of Figure 3, implying that the main information of the signal is contained in  $\phi_i \leq 22$  modes, which means that the initial condition  $u_N^0$  can be constructed with no more than 22 polynomial terms  $\phi_i$ . Again, if we observe Figure 2 (Right) and the values of Table 2, it emerges a strong correlation between the spatial convergence and the modal representation of Figure 3 (Right) already commented.

Otherwise, the source term presents more complications making necessary to refine the analysis. In contrast to the

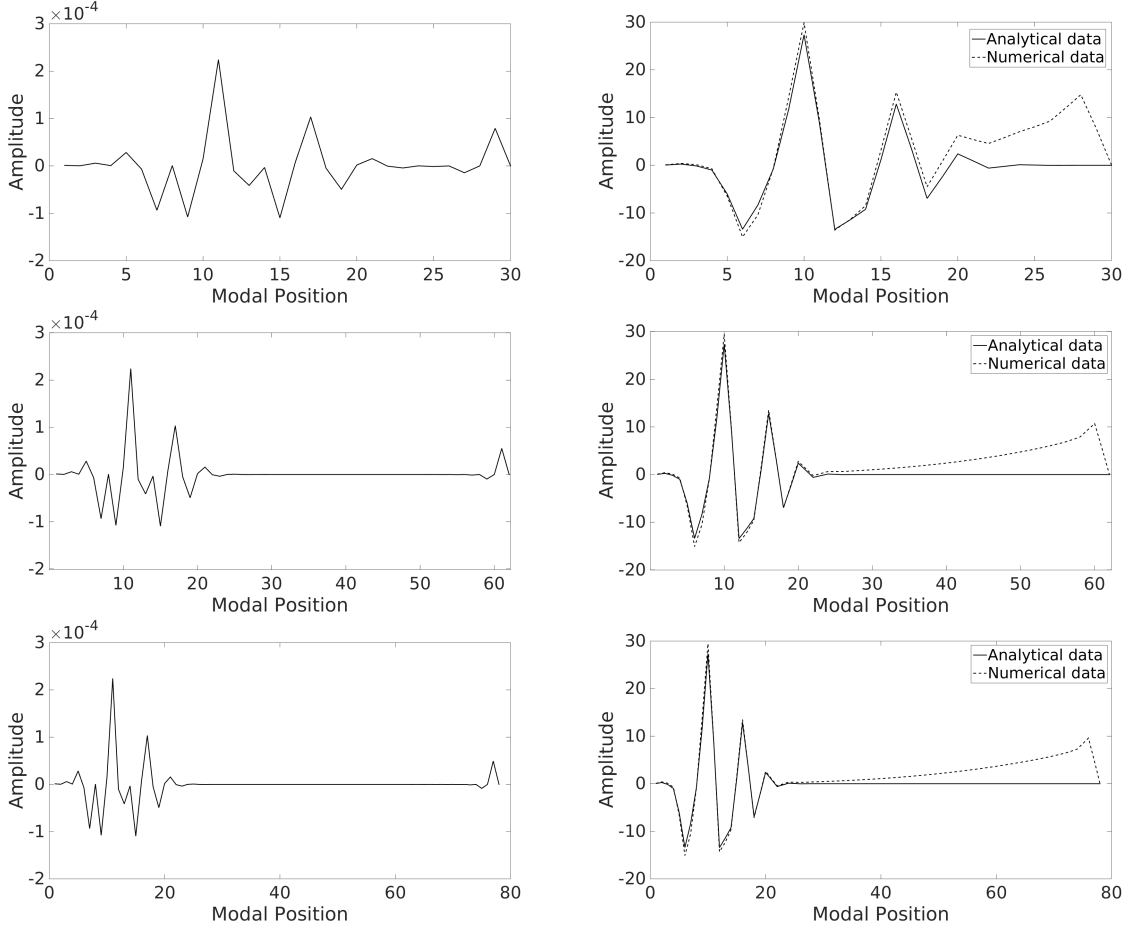


Figure 4: In all plots,  $\alpha = 1, \beta = 0.3$  and  $\Delta t = 10^{-5}$  seconds. Here, we check the temporal iteration  $k = 40$ . The number of polynomial terms used are (Top row)  $N = 32$ , (Center row)  $N = 64$  and (Bottom row)  $N = 80$ . (Left column) the modal representation of the projected source term  $\mathbf{CF}^{k+\frac{1}{2}}$ . (Right column) the numerical solution  $\hat{u}_n^{k+1}$  and the analytical solution (25) in the  $\phi$ -space.

initial condition, the source term (24) does not satisfy the boundary conditions stated onto the problem (1), since it is only defined at the interval  $(-1, 1)$ . We highlight this fact because by construction, the  $\phi$ -domain transformation between the source term  $f_N^{k+\frac{1}{2}}$  and the modal source  $\hat{f}_n^{k+\frac{1}{2}}$  only involves the homogeneous Dirichlet boundary conditions and not the Neumann conditions. Indeed, contrary to the spectrum of the initial condition, for the modal signal  $\hat{f}_n^{k+\frac{1}{2}}$ , i.e.,  $\mathbf{F}^{k+\frac{1}{2}}$ , the shape of their spectra always increases when  $N$  is varied, suggesting that they require of infinite modes in order to be fully characterized. Moreover, from (20)–(22), we observe that the modal vector  $\mathbf{F}^{k+\frac{1}{2}}$  is multiplied by the mass matrix,  $M$ , before it is introduced into the implementation scheme. Thus, the source term is transformed into a projected source term, namely,  $\mathbf{CF}^{k+\frac{1}{2}}$ . It is worth mentioning that the transformation of  $\mathbf{F}^{k+\frac{1}{2}}$  into the projected source term  $\mathbf{CF}^{k+\frac{1}{2}}$  provides similar spectra than Figure 3 (Right) but, in that case, they also contain an artifact that appears at high modes always close to  $N$ , independently of its value.

To illustrate this point, we present some results in Figure 4. All the plots are obtained through simulations with parameters  $\alpha = 1, \beta = 0.3$  and  $\Delta t = 10^{-5}$  seconds. Furthermore, we represent the data at the temporal iteration  $k = 40$ . The results represented in each row are obtained with  $N = 32$ ,  $N = 64$  and  $N = 80$  polynomial terms, respectively. Respect to the left column, this displays the results of three different modal spectra of  $\mathbf{CF}^{k+\frac{1}{2}}$ , whose modal distribution is concentrated in the same range of polynomial terms,  $\phi_i \leq 22$  modes. However, we clearly observe an artifact that always appears at the final modes of the plots, no matter the value of  $N$  is employed. It is important to inform that this

error has been deeply analyzed by numerical simulations obtaining the following conclusions. In addition, the case where the artifact is smaller is observed for  $\alpha = 1, \beta = 0$ , independent of  $\Delta t, N$ , meanwhile, for different values of  $\beta$  considerably worsen the results. Moreover, the artifact behaves as expected in the previous theory since, for either high values of  $N$  or small temporal steps, it tends to vanish. On the other hand, the right column shows the outputs  $\hat{u}_n^{k+1}$  (that is,  $\mathbf{U}^{k+1}$ ) and their corresponding analytical values, (25). In this one the analytical solutions are illustrated with solid lines, showing similar spectra than the initial data given in Figure 3 (Right). In all the cases, the signals are represented with no more than 22 polynomial terms independently of the  $N$  value and note that, for the rest of the temporal iterations  $k$ , the solution of the problem (25) may change the shape of the signal depending on the  $k$  value, but always preserving the limit  $\phi_i \leq 22$  polynomial terms previously noticed. Concerning the signals of  $\mathbf{U}^{k+1}$ , which are illustrated with dashed lines, these always differ from the analytical results in the high modal range presenting a strong correlation with the signals of  $\mathbf{CF}^{k+\frac{1}{2}}$  depicted in Figure 4 (Left column). We observe that the artifact generated in the projected source term ( $\mathbf{CF}^{k+\frac{1}{2}}$ ) is propagated into the numerical solution  $\mathbf{U}^{k+1}$  introducing numerical errors at high modes that are globally acquired in  $u_N^{k+1}$ .

### 3.3. Dispersion and diffusion parameters calibration

Once understood the behavior of the numerical approximation that has developed here, we are able to go one step forward and observe the influence of the dispersion and diffusion parameters in their whole ranges. As mentioned, the KdVB equation is considered to investigate the impact of bottom configurations on the free surface waves and describe a wide variety of phenomena arise in plasma physics, among others. Motivated by those applications and using as starting point the references [15, 26, 16, 22, 20, 21], in this subsection we develop three parametric configurations among the coefficients  $\alpha$  and  $\beta$ . Although several constant physics have been simplified in our analysis, all profiles below are consistent with the previous sections and the references above mentioned.

Henceforth, all color graphics display error estimates among the analytical and numerical solution for different parameter configurations. In addition, those errors are depicted in decibels (dBs)(i.e.,  $20 \log_{10} \epsilon$ ), where the color white represents regions with low-error values whereas dark color shows high numerical errors. In fact, errors around  $-85$  dBs mean that  $\epsilon \sim 5 \cdot 10^{-5}$ , whereas errors of  $-20$  dBs mean that  $\epsilon \sim 10^{-1}$ . Finally, all experiments have been carried out by considering  $N = 32$  nodes.

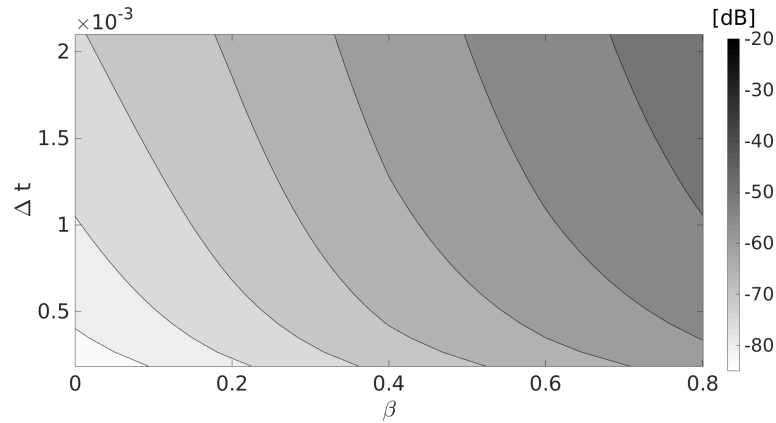


Figure 5: A color graph where the  $x$ -axis is the  $\beta$  parameter and the  $y$ -axis represents the different temporal steps  $\Delta t$ . Color white denotes low errors meanwhile dark regions mean high errors.

*First configuration* ( $\alpha = 1$  and  $\beta \in [0, 0.8]$ ). In this case we extend the analysis associated to the temporal convergence by considering a massive experiment where the accuracy (26) is again measured for time steps  $\Delta t$  in the range  $\{(i+1)10^{-4} : i = 1, \dots, 20\}$ . Moreover, the parameter  $\beta$  is defined in the range  $\{(i-1)4 \cdot 10^{-2} : i = 1, \dots, 20\}$ . Lastly, we fix the simulation time to  $T = 2$  seconds. Thus,  $20 \times 20$  ( $\beta \times \Delta t$ ) simulations are carried out when the dispersion coefficient is constant, namely,  $\alpha = 1$ . Figure 5 shows the results obtained throughout the massive numerical experiment described above.

In general terms, the results of the experiment seem reasonable and the spatial–temporal convergence of our approach is easily observed in a wide range between  $\beta$  and  $\Delta t$ . Note that there is a clear dependence in the errors from the dissipation coefficient  $\beta$ . Indeed, as observed in Theorem 2.2, the inclusion of a second order derivative in the KdV equation leads to a suboptimal convergence for either the temporal or spatial discretization. Besides, with this particular configuration among the dispersion and diffusion parameters, note that Figure 5 also exhibits a numerical perspective to the theoretical assumption H1 given in (14).

*Second configuration* ( $\alpha \in (0.2, 1.15]$ ,  $\beta \in [0.2, 0.65]$ ). We present another massive numerical experiment of  $20 \times 20$  simulations in Figure 6. To be more precise, the dispersion parameter  $\alpha$  belongs to the set  $\{0.2 + (i-1)5 \cdot 10^{-3} : i = 1, \dots, 20\}$  and the dissipation parameter  $\beta$  belongs to the set  $\{(i-1)3.25 \cdot 10^{-2} : i = 1, \dots, 20\}$ . Taking into account the above sets, we depicted two gray–scaled graphs where the color again represents the error ( see (26) with  $p = 2$ ) associated to the specific simulation computes. Figure 6 (Left) shows the results for  $\Delta t = 10^{-3}$  seconds and Figure 6 (Right) for  $\Delta t = 10^{-4}$  seconds.

Additionally, we have selected  $\alpha \in (0.2, 1.15]$  and  $\beta \in [0, 0.65]$  because we pretend to guarantee results with accuracy inside of the range of  $[-85, -20]$  dBs. Under these intervals, we present the error values in two different cases of  $\Delta t$ , as mentioned  $\Delta t = 10^{-3}$  and  $\Delta t = 10^{-4}$  seconds. Note that, in both graphs, the shape in the color variation is preserved whereas the amount of error in Figure 6 (Left) is constantly increased (i.e., homogeneously darker) than for the results of Figure 6 (Right) which errors are obtained with a smaller temporal discretization. We also highlight that, independently of the temporal step employed, values of  $\alpha < 0.2$  provide critical errors of  $\epsilon$ , which are out of the accuracy bounds previously established. Moreover, we also restrict the range of  $\beta$  to 0.65 because the errors become critical, i.e., up to  $-20$  dBs, if we consider simulations with a parameter  $\alpha < 1/3$ . To finish this case, it is worth pointing that these results are in full concordance with the established relation H1 among the dispersion and diffusion parameters.

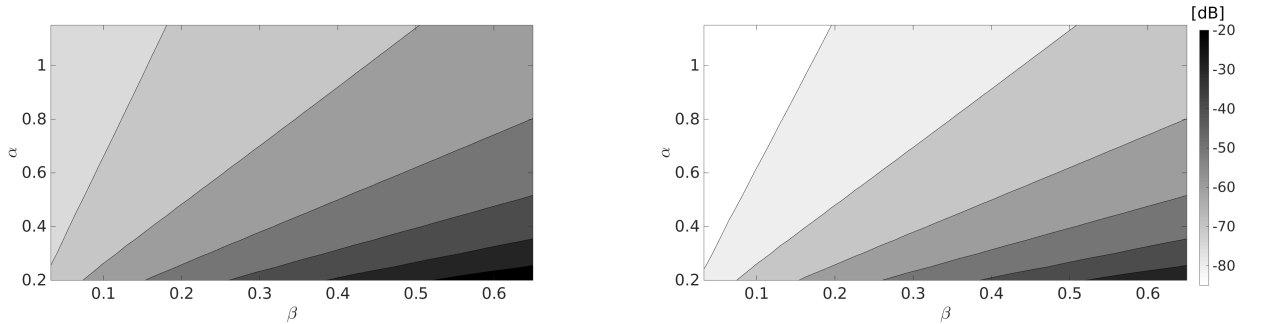


Figure 6: Color graphs where the  $x$ -axis is the  $\beta$  coefficient and the  $y$ -axis represents the different coefficients  $\alpha$ . Color white denotes low errors whereas dark regions mean high errors  $\epsilon$ . Two temporal steps are considered: (Left) Fixing  $\Delta t = 10^{-3}$  seconds and (Right) fixing  $\Delta t = 10^{-4}$  seconds.

*Third configuration* ( $\alpha$  and  $\beta$  with temporal–dependence). To conclude, we develop several experiments considering time–dependent parameters. As mentioned at the beginning of this section, the chosen temporal profiles are based upon the papers found in the literature. From [26] and [22] and by simplicity, some physical data have been modified. More precisely, we analyze the following two cases:

- *Case 1.*  $\alpha(t) = 5 \cos\left(\frac{\pi t}{4}\right)$ ,  $\beta(t) = \frac{1}{\cos\left(\frac{\pi t}{4}\right)}$ ,  $\forall t \in [0, 1]$ .
- *Case 2.*  $\alpha(t) = (t+1)^2$ ,  $\beta(t) = \frac{0.5}{t+1}$ ,  $\forall t \in [0, 1]$ .

In both cases, we introduce these parameters into the implementation scheme (20) and also considering the initial condition (23) and the source term (24). Recall that the  $\alpha$  and  $\beta$  profiles defined above explicitly appear in the source term (24), and whose solution (25) is free of the dispersion and diffusion parameters. As mentioned, these

specific conditions make possible to define a benchmark (26), which is either absolute or representative measure to fit the accuracy of these time–variation parameters into the numerical scheme (20). Therefore, we compute the error,  $\epsilon$ , in each case by using three different temporal samplings,  $\Delta t = \{10^{-2}, 10^{-3}, 10^{-4}\}$  seconds. Moreover, we define two measures that give proper error bounds useful to easily calibrate the accuracy of the scheme when those time–dependent parameters are used. Therefore, we define both, the upper and the lower bound by considering the theoretical assumption H1 (see theorem 2.2) as well as the numerical results from Figure 6. Briefly speaking, the main idea consists in providing a reliable error interval that permits to establish a simple calibration of the method through simulations with constant parameters. To do that, we define the upper error, denoted by  $\epsilon_{max}$ , and the lower error, denoted by  $\epsilon_{min}$ , by considering the constant pairs  $(\bar{\alpha}, \bar{\beta})$  that make maximum (resp. minimum) the error  $\epsilon$ . Note that these pairs  $(\bar{\alpha}, \bar{\beta})$  would strongly depend on the profile defined and their values would be different at each case treated. For example, if we consider the Case 1, the maximum error,  $\epsilon_{max}$ , is obtained when  $\bar{\alpha} = 5/\sqrt{2}$  and  $\bar{\beta} = \sqrt{2}$ , whereas the minimum error,  $\epsilon_{min}$  occurs for  $\bar{\alpha} = 5$  and  $\bar{\beta} = 1$ . For the Case 2,  $\epsilon_{max}$  is obtained with a simulation with  $\bar{\alpha} = 1$  and  $\bar{\beta} = 0.5$ , whereas  $\epsilon_{min}$  is achieved when  $\bar{\alpha} = 4$  and  $\bar{\beta} = 0.25$ .

Table 3: Analysis of the error,  $\epsilon$  and the upper and lower-bound error,  $\epsilon_{max}$  and  $\epsilon_{min}$  respectively. The three quantities are measured considering 1 second of time simulation and  $N = 32$  nodes.

Case 1	$\Delta t = 10^{-4}$	$\Delta t = 10^{-3}$	$\Delta t = 10^{-2}$	Case 2	$\Delta t = 10^{-4}$	$\Delta t = 10^{-3}$	$\Delta t = 10^{-2}$
$\epsilon_{max}$	0.00070345	0.00220118	0.00744720	$\epsilon_{max}$	0.00027205	0.00087034	0.00322214
$\epsilon_{min}$	0.00018275	0.00059578	0.00251925	$\epsilon_{min}$	0.00005478	0.00019861	0.00134123
$\epsilon$	0.00029501	0.00095356	0.00341955	$\epsilon$	0.00009874	0.00032937	0.00181271

The  $\epsilon$  results of both cases and their corresponding error bounds,  $\epsilon_{max}$  and  $\epsilon_{min}$ , are recorded in Table 3 considering three different temporal steps. It is worth pointing out that the results exhibit in Table 3 are in full concordance with the previous explanations and the error,  $\epsilon$ , is always within the error interval  $[\epsilon_{min}, \epsilon_{max}]$ , no matter which temporal step is employed.

#### 4. Conclusions

The linear KdVB equation with non–periodic boundary conditions and time–dependent coefficients has been numerically analyzed using the LPG method for the spatial discretization, and a finite difference scheme for the temporal behavior. The core of our analysis are new estimates related to the stability and convergence problems for this kind of equations, which now involve non constant coefficients. Specifically, the convergence result proved in Theorem 2.2 shown a trade off between dispersion and diffusion parameters added into the model with a view to establishing upper estimates in the form  $C_\alpha(N^{-r} + (\Delta t)^2) + C_\beta(N^{1-r} + (\Delta t)^2)$ , where  $C_\alpha \approx (\min \alpha(t))^{-1}$ ,  $C_\beta \approx \|\beta\|_{L^\infty([0,T])}$  and  $r \geq 2$ . Respect to the stability, it can swing sharply if the dispersion coefficient  $\alpha(t)$  is small enough, see Theorem 2.1.

The computed results of the KdVB equation (1) exhibit the high accuracy of the proposed method based in the Euler scheme–LPG approximation. First, we have define a proper benchmark (26), which is based on the data (23)–(24), providing evidences of the theoretical results in the temporal and spatial convergence. Moreover, we complement the analysis of the spatial convergence pointing out the relation between the numerical error and the projected source term,  $\mathbf{CF}$ . Secondly, we develop a wide numerical analysis of the  $\alpha(t)$  and  $\beta(t)$  parameters. Finally, we present several experiments that show the best performance ranges and the proper calibration of time–dependent profiles.

To the best of our knowledge, our framework constitutes a first approach for studying from a numerical point of view dynamic systems of odd–order dispersive equations with coefficients that can vary in time. The results obtained in this paper shown the role and trade off of these temporal parameters into the model.

Finally, there are many ways to extend these ideas to future works. For example, a first future work could consider nonlinearity into the model (1) with its respective coefficient, and it is associated to the convective term  $\gamma(t)uu_x$ , with  $\gamma(t) \neq \alpha(t)$ ,  $\gamma(t) \neq \beta(t)$ . Nevertheless, it worth mentioning that the nonlinear analysis requires additional techniques that are not considered in this work. We invite readers to review the references for more details on the nonlinear case. For this kind of systems, a details comparison of the LPG approach to other methods in terms of accuracy and efficiency would also be of interest. In a more general sense, similar ideas may also be fruitful in considering evolution dynamics described by PDEs including time parametric dependencies located in its coefficients.



## References

- [1] Ali H. Bhrawy and M. M. Al-Shomrani. A Jacobi dual-Petrov Galerkin-Jacobi collocation method for solving Korteweg-de Vries equations. *Abstr. Appl. Anal.*, pages Art. ID 418943, 16, 2012.
- [2] J. L. Bona and M. E. Schonbek. Travelling-wave solutions to the Korteweg-de Vries-Burgers equation. *Proc. Roy. Soc. Edinburgh Sect. A*, 101(3-4):207–226, 1985.
- [3] J. M. Burgers. Application of a model system to illustrate some points of the statistical theory of free turbulence. *Nederl. Akad. Wetensch., Proc.*, 43:2–12, 1940.
- [4] Claudio Canuto, M. Yousuff Hussaini, Alfio Quarteroni, and Thomas A. Zang. *Spectral methods in fluid dynamics*. Springer Series in Computational Physics. Springer-Verlag, New York, 1988.
- [5] Dumitru I. Caruntu. Classical Jacobi polynomials, closed-form solutions for transverse vibrations. *J. Sound Vibration*, 306(3-5):467–494, 2007.
- [6] Zhenguang Deng and Heping Ma. Optimal error estimates of the Fourier spectral method for a class of nonlocal, nonlinear dispersive wave equations. *Appl. Numer. Math.*, 59(5):988–1010, 2009.
- [7] E. H. Doha, W. M. Abd-Elhameed, and A. H. Bhrawy. Efficient spectral ultraspherical-Galerkin algorithms for the direct solution of  $2n$ th-order linear differential equations. *Appl. Math. Model.*, 33(4):1982–1996, 2009.
- [8] E. H. Doha, A. H. Bhrawy, and W. M. Abd-Elhameed. Jacobi spectral Galerkin method for elliptic Neumann problems. *Numer. Algorithms*, 50(1):67–91, 2009.
- [9] E. H. Doha, A. H. Bhrawy, and R. M. Hafez. A Jacobi-Jacobi dual-Petrov-Galerkin method for third- and fifth-order differential equations. *Math. Comput. Modelling*, 53(9-10):1820–1832, 2011.
- [10] Eid H. Doha and Ali H. Bhrawy. A Jacobi spectral Galerkin method for the integrated forms of fourth-order elliptic differential equations. *Numer. Methods Partial Differential Equations*, 25(3):712–739, 2009.
- [11] Jinwei Fang, Boying Wu, and Wenjie Liu. An explicit spectral collocation method for the linearized Korteweg–de Vries equation on unbounded domain. *Appl. Numer. Math.*, 126:34–52, 2018.
- [12] Zhaosheng Feng and Roger Knobel. Traveling waves to a Burgers-Korteweg-de Vries-type equation with higher-order nonlinearities. *J. Math. Anal. Appl.*, 328(2):1435–1450, 2007.
- [13] J. D. Fenton and M. M. Rienecker. A Fourier method for solving nonlinear water-wave problems: application to solitary-wave interactions. *J. Fluid Mech.*, 118:411–443, 1982.
- [14] B. Fornberg and G. B. Whitham. A numerical and theoretical study of certain nonlinear wave phenomena. *Philos. Trans. Roy. Soc. London Ser. A*, 289(1361):373–404, 1978.
- [15] Xin-Yi Gao. Variety of the cosmic plasmas: general variable-coefficient Korteweg-de Vries-Burgers equation with experimental/observational support. *EPL (Europhysics Letters)*, 110(1):15002, 2015.
- [16] Xin-Yi Gao. Mathematical view with observational/experimental consideration on certain  $(2+1)$ -dimensional waves in the cosmic/laboratory dusty plasmas. *Appl. Math. Lett.*, 91:165–172, 2019.
- [17] David Gottlieb and Steven A. Orszag. *Numerical analysis of spectral methods: theory and applications*. Society for Industrial and Applied Mathematics, Philadelphia, Pa., 1977. CBMS-NSF Regional Conference Series in Applied Mathematics, No. 26.
- [18] David Gottlieb and Chi-Wang Shu. On the Gibbs phenomenon and its resolution. *SIAM Rev.*, 39(4):644–668, 1997.
- [19] Olivier Goubet and Jie Shen. On the dual Petrov-Galerkin formulation of the KdV equation on a finite interval. *Adv. Differential Equations*, 12(2):221–239, 2007.
- [20] Jiu-Ning Han, Jun-Hua Luo, and Jun-Xiu Li. Nonlinear electrostatic coherent structures: solitary and shock waves in a dissipative, nonplanar multi-component quantum plasma. *Astrophysics and Space Science*, 349(1):305–315, 2014.
- [21] S Hussain and S Mahmood. Korteweg-de vries burgers equation for magnetosonic wave in plasma. *Physics of Plasmas*, 18(5):052308, 2011.
- [22] Nusrat Jehan, Arshad M Mirza, and M Salahuddin. Planar and cylindrical magnetosonic solitary and shock waves in dissipative, hot electron-positron-ion plasma. *Physics of Plasmas*, 18(5):052307, 2011.
- [23] Alper Korkmaz. Numerical algorithms for solutions of Korteweg-de Vries equation. *Numer. Methods Partial Differential Equations*, 26(6):1504–1521, 2010.
- [24] D. J. Korteweg and G. de Vries. On the change of form of long waves advancing in a rectangular canal, and on a new type of long stationary waves. *Philos. Mag. (5)*, 39(240):422–443, 1895.
- [25] Jian Li, Heping Ma, and Weiwei Sun. Error analysis for solving the Korteweg-de Vries equation by a Legendre pseudo-spectral method. *Numer. Methods Partial Differential Equations*, 16(6):513–534, 2000.
- [26] Jian-Guo Liu, Wen-Hui Zhu, Li Zhou, and Yao-Kun Xiong. Multi-waves, breather wave and lump–stripe interaction solutions in a  $(2+1)$ -dimensional variable-coefficient Korteweg–de Vries equation. *Nonlinear Dynamics*, 97(4):2127–2134, 2019.
- [27] Heping Ma and Weiwei Sun. A Legendre-Petrov-Galerkin and Chebyshev collocation method for third-order differential equations. *SIAM J. Numer. Anal.*, 38(5):1425–1438, 2000.
- [28] Heping Ma and Weiwei Sun. Optimal error estimates of the Legendre-Petrov-Galerkin method for the Korteweg-de Vries equation. *SIAM J. Numer. Anal.*, 39(4):1380–1394, 2001.
- [29] Y. Maday and A. Quarteroni. Error analysis for spectral approximation of the Korteweg-de Vries equation. *RAIRO Modél. Math. Anal. Numér.*, 22(3):499–529, 1988.
- [30] Wilfried Philips and Geert De Jonghe. Data compression of ecg’s by high-degree polynomial approximation. *IEEE transactions on biomedical engineering*, 39(4):330–337, 1992.
- [31] Yonghui Qin and Heping Ma. Legendre-tau-Galerkin and spectral collocation method for nonlinear evolution equations. *Appl. Numer. Math.*, 153:52–65, 2020.
- [32] Jie Shen. Efficient spectral-Galerkin method. I. Direct solvers of second- and fourth-order equations using Legendre polynomials. *SIAM J. Sci. Comput.*, 15(6):1489–1505, 1994.

- [33] Jie Shen. A new dual-Petrov-Galerkin method for third and higher odd-order differential equations: application to the KdV equation. *SIAM J. Numer. Anal.*, 41(5):1595–1619, 2003.
- [34] Gabor Szegő. *Orthogonal Polynomials*. American Mathematical Society, New York, 1939. American Mathematical Society Colloquium Publications, v. 23.
- [35] Daniel Tchiotop, Didier Wolf, Valerie Louis-Dorr, and Rene Husson. Ecg data compression using jacobi polynomials. In *2007 29th Annual International Conference of the IEEE Engineering in Medicine and Biology Society*, pages 1863–1867. IEEE, 2007.
- [36] Houria Triki and Abdul-Majid Wazwaz. Traveling wave solutions for fifth-order KdV type equations with time-dependent coefficients. *Commun. Nonlinear Sci. Numer. Simul.*, 19(3):404–408, 2014.
- [37] Pengfei Wang and Pengzhan Huang. Convergence of the Crank-Nicolson extrapolation scheme for the Korteweg–de Vries equation. *Appl. Numer. Math.*, 143:88–96, 2019.
- [38] Xin Yu, Yi-Tian Gao, Zhi-Yuan Sun, and Ying Liu. Solitonic propagation and interaction for a generalized variable-coefficient forced Korteweg–de Vries equation in fluids. *Physical Review E*, 83(5):056601, 2011.
- [39] Juan-Ming Yuan and Jiahong Wu. A dual-Petrov-Galerkin method for two integrable fifth-order KdV type equations. *Discrete Contin. Dyn. Syst.*, 26(4):1525–1536, 2010.